

Roles of Oxygen Vacancies of CeO₂ and Mn-doped CeO₂ with the same morphology in Benzene Catalytic Oxidation

Min Yang¹, Genli Shen², Qi Wang², Ke Deng², Mi Liu², Yunfa Chen³, Yan Gong^{2, *}, Zhen Wang^{2, *}

¹ School of Chemistry and Biological Engineering, University of Science and Technology Beijing, 100083, China; yangmin@ustb.edu.cn (M. Y.)

² CAS Key Laboratory of Standardization and Measurement for Nanotechnology, CAS Center for Excellence in Nanoscience, National Center for Nanoscience and Technology, Beijing 100190, China; shengl@nanoctr.cn (G.S.); wangq@nanoctr.cn (Q.W.); kdeng@nanoctr.cn (K.D.); liumi@nanoctr.cn (M.L.);

³ State Key Laboratory of Multiphase Complex Systems, Institute of Process Engineering, Chinese Academy of Sciences, Beijing 100190, China; yfchen@home.ipe.ac.cn

* Correspondence: wangzh@nanoctr.cn (Z.W.); gongyan@nanoctr.cn (Y.G.); Tel.: +86-10-82545755; Fax: +86-10-62525716

Abstract: Mn-doped CeO₂ and CeO₂ with the same morphology (nanofiber and nanocube) were synthesized through hydrothermal method respectively. When applied to benzene oxidation, the catalytic properties of Mn-doped CeO₂ were higher than those of CeO₂, which was related with the concentration of O vacancy. Compared to CeO₂ with the same morphology, more oxygen vacancies were formed on the surface of Mn-doped CeO₂, due to Mn ion replacing Ce ion. The lattice replacement was analyzed through XRD, Raman, electron energy loss spectroscopy and electron paramagnetic resonance technology. The formation energies of oxygen vacancy on the different exposed crystal planes [(110) and (100)] for Mn-doped CeO₂ were calculated by applying the density functional theory (DFT). The data showed that the oxygen vacancy was easier to be formed on the (110) plane. The factors influencing catalytic behavior were elaborated, which indicated that surface oxygen vacancy played an important part in catalytic reaction.

Keywords: Mn-doped CeO₂; pure CeO₂; morphology; oxygen vacancy; benzene oxidation

1. Introduction

Volatile organic compounds (VOCs) are a type of low-boiling point organic matter which contains aromatic hydrocarbons, straight-chain alkane and cycloalkanes, etc [1]. VOCs can be produced in industrial process and daily life and bring harm to human health and environment. Hence, it is particularly urgent to limit VOC emissions [2]. There are many methods to remove VOCs, in which catalytic oxidation is considered to be the most effective method due to its destructive efficiency, lower operating temperature and less by-products [3, 4]. At present, two types of common catalysts have been widely researched: one is precious metal type and the other is transition metal oxide type. The application of former is limited due to the cost, sintering risk and facile poisoning. In contrast, the transition metal oxide is attracting more attention owing to the high-stability, low cost and high oxidation activity at low temperatures [5-7]. In recently years, transition metal based oxides catalysts exhibited excellent catalytic behaviors towards the removal of VOCs, such as Mn-based [8-10] and Co-based [11, 12] metal oxide catalysts.

Additionally, rare-earth oxides have also attracted wide attention over the VOCs catalytic oxidation. CeO₂, as typical rare earth oxide has been investigated in the field of heterogeneous catalysis and exhibits enhanced performances for VOC oxidation due to its outstanding redox

property and oxygen storage capacity (OSC). It is worthy to note that the microstructure of CeO₂ is closely related with the catalytic activity, especially crystal plane defects. Trovarelli and Llorca [13] reported different planes of CeO₂ possessed different content of oxygen vacancy. The activity of CeO₂ for VOC oxidation is sensitive to the proportion of surface oxygen defects in the catalyst [14]. Once the surface active oxygen vacancies are covered by intermediates or carbon deposition, the catalytic behavior of CeO₂ will be poisoned [15, 16]. In order to increase the content of active sites, transition metals are often used to be doped or composited with CeO₂ to produce more oxygen vacancies. Among the transition metals doped catalysts, Mn-based catalysts are widely used in the field of environmental catalysis [17, 18]. It is reported that Mn-doped CeO₂ has been applied in the abatement of contaminants, such as the catalytic reduction of NO and diesel soot combustion, which exhibit excellent catalytic activity [19–23].

In this article, we investigate the catalytic behavior of pure CeO₂ and Mn-doped CeO₂ with the same morphology through the complete catalytic oxidation of benzene. Their catalytic activities differences and crystal structures are analyzed in detail. Meanwhile, density function theory (DFT) was adopted to simulate crystal plane structure and calculate the formation energy of oxygen vacancies on the certain exposed plane. Although the effect of oxygen vacancy in pure CeO₂ on the catalytic property has been recognized, however the influence of dopants in oxygen vacancy for doped CeO₂ need to be described further. In addition, the formation difference of oxygen vacancy on the different exposed crystal plane is also less reported. Therefore, the main aim of our research is to discuss the effect of crystal plane structure and dopant (Mn ion) dispersion on the formation of oxygen vacancy and analyze the roles of oxygen vacancy in the combustion of benzene further.

2. Materials and Methods

2.1 The preparation of CeO₂-MnO_x composite oxides

The chemicals used in this work, including Ce(NO₃)₃·6H₂O (99%), Mn(NO₃)₂ solution (50%), NaOH (98%), and ethanol, were purchased from Beijing Chemicals Company (Beijing, China). Mn-doped CeO₂ with different morphologies (nanofiber: NF and nanocube: NC) were synthesized by a hydrothermal process. Firstly, Ce(NO₃)₃·6H₂O and Mn(NO₃)₂ in appreciate amounts (Ce/Mn mole ratio=9/1) were dissolved in a 10 mL H₂O and mixed with a 6 M NaOH solution. The solution was stirred for 0.5h at room temperature then transferred to an autoclave (100 mL) and gradually heated to a certain temperature (NF corresponding to 120 °C, NC corresponding to 160 °C). The given temperature was kept for 24 h. After the reaction, the precipitates in autoclaves were collected by centrifugation, washed with distilled water and ethanol several times. The obtained materials, labeled as Ce-Mn-NF and Ce-Mn-NC respectively, were dried at 80 °C overnight and calcined at 550 °C for 4 h. Pure CeO₂ with fiber and cube morphology were also prepared using the similar process as reference, labeled as CeO₂-NF and CeO₂-NC respectively.

2.2 Characterization technique

The crystal phases of the catalysts were characterized by X-ray diffraction (XRD) using Philips X'pert PRO analyzer (Philips, Amsterdam, The Netherlands) equipped with a Cu K α radiation source ($\lambda=0.154187$ nm) at a scanning rate of 0.03 °/s (2 θ from 10 ° to 90 °).

Scanning electron microscopy (SEM JC-Zeiss Merlin) and Transmission electron microscopy (TEM Tecnai G2 F20 U-TWIN) was used to observe the morphology and structure of samples.

Aberration-corrected HAADF-STEM images, Mn L2,3-edge and Ce M4,5-edge electron energy loss spectroscopy (EELS) were performed from FEI Titan electron microscope equipped with a Gatan Enfium camera system.

The surface composition and chemical states were determined by X-ray photoelectron spectroscopy (XPS ESCALAB250Xi). The binding energy (BE) was calibrated using the C1s line at 284.8 eV.

Raman spectra were measured with a Raman spectrometer (Renishaw inVia plus). The excitation source was an Ar⁺ ion laser ($\lambda = 514.23$ nm) and the laser power was 20 mW.

Reactive oxygen species were identified by the electron paramagnetic resonance technology (EPR) at room temperature on a Bruker EMX spectrometer (Bruker Corp., USA) at a frequency of 9.8 GHz and a magnetic field of 100 kHz.

Hydrogen temperature-programmed reduction (H₂-TPR) was performed on AutoChem 2920 chemisorption analyzer. Firstly, the sample (40–60 mesh) was heated to 150 °C and maintained at this temperature for 1h in 5% O₂ and 95% He mixture (30 mL/min), and then cooled to 50 °C under He flow. The samples were then heated again to 900 °C in 10% H₂ and 90% Ar mixture (50 mL/min).

The heating rate is 10 °C/min. The thermal conductivity detector signal was detected.

2.3 Catalytic activity tests

Activity tests for catalytic oxidation of benzene over CeO₂-NF, CeO₂-NC, Ce-Mn-NF and Ce-Mn-NC catalysts were performed in a continuous-flow fixed-bed reactor, containing 100 mg catalyst samples (40–60 mesh), respectively. The total reactant flow rate was 100 mL·min⁻¹, containing (100 ppm benzene+20 vol% O₂ + N₂ (balance)). The weight hourly space velocity (WHSV) was typically 60,000 mL·g⁻¹·h⁻¹. The concentrations of Benzene, CO₂, and CO were analyzed on-line using a gas GC/MS ((Hewlett-Packard 6890N and Hewlett-Packard 5973N). 5.0 vol% water vapor was introduced to the system by a water saturator at 34 °C. Catalytic activities were characterized by two parameters (T₅₀ and T₉₀). For a catalyst, T₅₀ and T₉₀ represents the temperature of 50 and 90% benzene conversion, respectively. The benzene conversion and CO₂ selectivities are calculated as following equations (1) and (2). [Benzene]_{in} and [Benzene]_{out} are the inlet and outlet Benzene concentrations during catalytic reaction):

$$\text{Benzene conversion (\%)} = \frac{[\text{Benzene}]_{in} - [\text{Benzene}]_{out}}{[\text{Benzene}]_{in}} \times 100\% \quad (1)$$

$$\text{CO}_2 \text{ selectivity (\%)} = \frac{[\text{CO}_2]}{([\text{CO}] + [\text{CO}_2])} \times 100\% \quad (2)$$

2.4 Details of DFT+U Calculation

First-principles calculations based on density functional theory (DFT) were carried out with the Vienna Ab-initio simulation package (VASP) and PBE functional. The interaction between core electrons and valence electrons was expressed by the projector-augmented wave (PAW) method. The cutoff energy of the plane-wave basis set was set to 550 eV. To guarantee the accuracy, the convergence criteria of energy and force were set to 10⁻⁵ eV and 0.05 eV·Å⁻¹, respectively. DFT+U

with $U = 5\text{eV}$ was applied to treat Ce 4f orbital. A model was built based on a $2 \times 2 \times 2$ CeO₂ supercell. The Brillouin zone of (100) and (110) models were sampled by a $3 \times 3 \times 1$ k-point set to acquire similar sampling densities. Before calculation, no more than half of the atomic layers from the bottom were fixed.

3. Results and Discussion

3.1 Catalytic oxidation activity over benzene

The catalytic activities of Mn-doped CeO₂ and pure CeO₂ with the same morphology were comparatively researched through the oxidation of benzene (Figure 1a). In the pattern, it can be obtained that the Ce-Mn-NF exhibits the best catalytic ability followed by Ce-Mn-NC, while CeO₂-NC possesses the least activity. T_{50} and T_{90} on Ce-Mn-NF is 278 and 395 °C respectively, which are much lower than those on Ce-Mn-NC (304/450 °C) and pure phase oxide. The catalytic activities of the catalysts were also compared based on the yield of CO₂. From the Figure 1b, it can be also obtained that the catalytic properties of Mn-doped CeO₂ are enhanced compared with CeO₂ with the same morphology. Meanwhile benzene has almost been converted into CO₂ completely without the detection of any other gas. Water vapor is a common component of industrial waste gas, therefore the impact of water vapor on catalytic activity is requisite. The impact of 5.0 vol% water vapor introduction on catalytic activities of Ce-Mn-NC and Ce-Mn-NF at 400 °C was conducted (Figure 1c and 1d). As a result, introduction of 5.0 vol% water vapor led to benzene conversion decreasing of Ce-Mn-NC and Ce-Mn-NF from 91% to 77% and 83% to 67%, respectively. After continuous 5.0 vol% water vapor injection for 10 hours, water was cut off, and the benzene conversions of Ce-Mn-NC and Ce-Mn-NF were restored. The competitive adsorption of H₂O and target benzene molecules at the active sites is the main reason of benzene conversion decreasing. The result above indicated both of Ce-Mn-NC and Ce-Mn-NF presented good water-resistant ability.

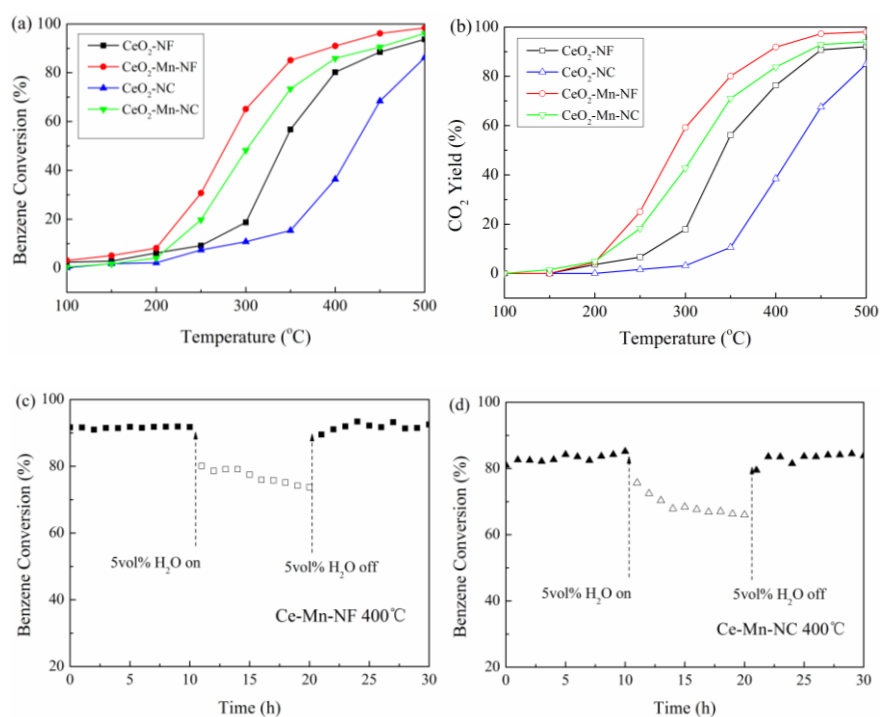


Figure 1. Benzene conversion (%), CO_2 yield (%) over $\text{CeO}_2\text{-NF}$, $\text{CeO}_2\text{-NC}$, Ce-Mn-NF and Ce-Mn-NC . Effect of water vapor on the catalytic activities of Ce-Mn-NF (c) and Ce-Mn-NC (d). Water concentration=5vol%.

3.2 Characterization of catalysts

The crystal structures of $\text{CeO}_2\text{-NF}$, $\text{CeO}_2\text{-NC}$, Ce-Mn-NF and Ce-Mn-NC was examined through XRD. From the pattern (Figure 2a), it can be obtained that the diffraction peaks at $2\theta = 28.5^\circ$, 33.0° , 47.4° , 56.4° , 59.2° , 69.5° , 76.6° , 79.1° and 88.6° in the XRD profile of the pure cerium oxide clearly demonstrate the presence of cubic fluorite structure of CeO_2 (PDF# 81-0792). For Mn-doped CeO_2 (Ce-Mn-NF and Ce-Mn-NC), the patterns do not show any diffraction of manganese oxides, and only broad reflections are observed, which should be attributed to the formation of Ce-O-Mn solid solution. It is worthy to note that the characteristic diffraction peak of CeO_2 ($2\theta=28.5^\circ$) in the Mn-doped CeO_2 is hardly shifted to higher values of the Bragg angles, compared with the pure CeO_2 , which may be related with the low content of Mn (Figure 2b).

The lattice parameters of all the samples have been calculated according to the XRD data and listed in Table 1. The result shows that the lattice parameters of the Mn-doped CeO_2 are lower than those of pure CeO_2 with the same morphology. The ionic radius of Mn^{n+} (Mn^{2+} (0.067nm), Mn^{3+} (0.066 nm) and Mn^{4+} (0.053nm)) are all smaller than that of the Ce^{4+} (0.1098 nm). Therefore, the incorporation of Mn^{n+} into the CeO_2 lattice to form Ce-O-Mn solid solution could result in lattice parameter decrease, which could lead to more proportion of oxygen vacancies.

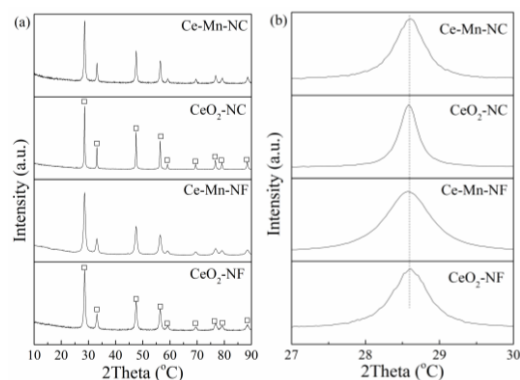


Figure 2. XRD patterns of $\text{CeO}_2\text{-NF}$, $\text{CeO}_2\text{-NC}$, Ce-Mn-NF and Ce-Mn-NC : (a) wild angle patterns, and (b) Enlarged-zone patterns.

Table 1 Lattice parameters and extent of deviation of synthesized samples.

Samples	Lattice parameters (a) (Å)	Extent of deviation (*10 ⁻⁴)
$\text{CeO}_2\text{-NF}$	5.40864	10.06
Ce-Mn-NF	5.40842	11.94
$\text{CeO}_2\text{-NC}$	5.41061	4.02
Ce-Mn-NC	5.40878	11.52

The morphology and structure of samples were characterized by SEM and TEM, respectively. Figure 3a shows the SEM image of $\text{CeO}_2\text{-NF}$. It can be seen that $\text{CeO}_2\text{-NF}$ with a fiber morphology has an average diameter of about 10 nm and length of about 150–300 nm. In the HRTEM of $\text{CeO}_2\text{-NF}$ (Figure 3b), the exposed crystal planes (110) and (100) can be determined obviously

according to the interplanar distance 0.19nm and 0.27nm, respectively. Additionally, (111) plane is also obtained inside the lattice. Figure 3c shows the SEM image of CeO₂-NC. The size of CeO₂-NC possessing cubic morphology is about 12–25 nm. Through the HRTEM (Figure 3d), it can be acquired that the exposed crystal plane is only (100). (111) plane also exists inside the lattice. For Ce-Mn-NF and Ce-Mn-NC, the morphology has no change compared with pure CeO₂ with the same morphology except the change of sample size (Figure 3e-3h). In order to analyze the element distribution of Mn-doped CeO₂, the HAADF mapping image of Ce-Mn-NF and Ce-Mn-NC were examined, respectively (Figure 3i and 3j). The result exhibits that the Ce and Mn elements are composited together homogeneously, which is useful to the oxygen vacancy formation.

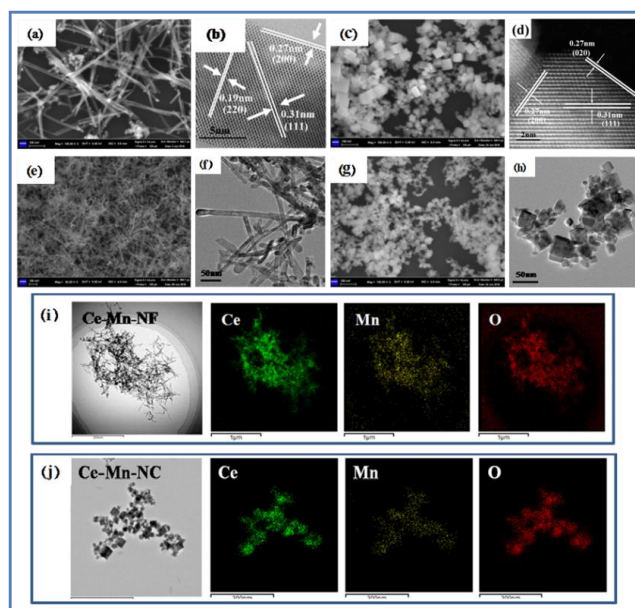


Figure 3. SEM and HRTEM images of CeO₂-NF and CeO₂-NC (a-d); SEM and TEM images of Ce-Mn-NF and Ce-Mn-NC (e-h); HAADF mapping images of Ce-Mn-NF and Ce-Mn-NC (i and j).

Raman scattering was used to identify the solid solution phase. Figure 4 shows visible Raman spectra of all the samples. In the pattern, a strong peak at ca. 460 cm⁻¹ and a weak one at ca. 610 cm⁻¹ are discerned, corresponding to the fluorite F_{2g} mode and a defect-induced mode (D mode), respectively [27, 28]. The peaks at 275 and 1163 cm⁻¹ are assigned to second-order transverse and longitudinal vibration modes of cubic CeO₂ fluoride phase [29]. These bands at ca. 610 cm⁻¹ are usually assigned to the presence of extrinsic oxygen vacancies created as charge compensating defects during solid solution formation [30]. For Ce-Mn-NF and Ce-Mn-NC, a band at ca. 610 cm⁻¹ corresponds to the second-order Raman mode attributes of O²⁻ vacancies formed by a low valence dopant (Mnⁿ⁺). For pure CeO₂, Raman band is also detected at ca. 610 cm⁻¹, which is also assigned to the presence of oxygen vacancies resulted from Ce⁴⁺ transforming to Ce³⁺. The ratio of integrated peak area of oxygen vacancy (~610 cm⁻¹) to that of main peak (460 cm⁻¹), defined as A₆₁₀/A₄₆₀, is used here to characterize the relative amount of oxygen vacancy among these samples. The A₆₁₀/A₄₆₀ ratio was calculated and ranked in the order of Ce-Mn-NF > Ce-Mn-NC > CeO₂-NF > CeO₂-NC (Table 2), suggesting that Ce-Mn-NF exhibits the higher concentration of oxygen vacancies. In other words, more Mn ions are doped into CeO₂-NF to form Ce-Mn-NF. This phenomenon is in agreement with the catalytic oxidation of benzene data, which indicate the oxygen vacancy is closely related with

the catalytic activity.

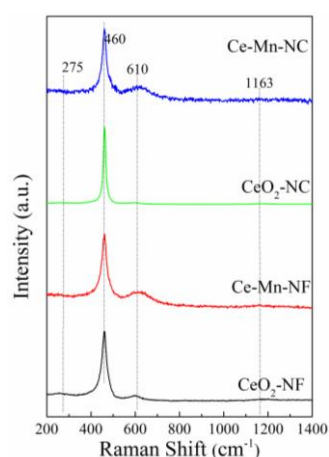


Figure 4. Room temperature visible Raman spectra of all the samples.

The oxidation state of catalyst surface species was examined by XPS analysis. Figure 5a presents the XPS spectra of the Ce 3d core levels for all samples. The peaks V_0/V_0' , V_1/V_1' and V_2/V_2' refer to three pairs of spin-orbit doublets, which can be attributed to surface Ce^{4+} [24, 31], while U_0/U_0' and U_1/U_1' can be ascribed to Ce^{3+} [32]. The relative amount of Ce^{3+} for all the samples can be calculated according to the equation (3) and listed in Table 2. The result shows that the relative atomic ratio of $Ce^{3+}/(Ce^{3+}+Ce^{4+})$ in the Ce-Mn-NF is higher than that of CeO₂-NF. The amount of Ce^{3+} in the Ce-Mn-NC is also higher than that of CeO₂-NC. The data indicate that the introduction of Mn ion can increase the relative amount of Ce^{3+} in the Mn-doped CeO₂, which might arise from the charge rebalancing of oxygen vacancies and dopant Mn^{n+} [33].

$$X_{Ce^{3+}} = \frac{A_{Ce^{3+}}/S_{Ce}}{\sum A_{(Ce^{3+}+Ce^{4+})}/S_{Ce}} \times 100\% \quad (3)$$

where $X_{Ce^{3+}}$ is the percentage content of Ce^{3+} , A is the integrate area of characteristic peak in the XPS pattern, S is sensitivity factors ($S=7.399$).

Figure 5b depicts the O 1s XPS spectra of the CeO₂-NF, CeO₂-NC, Ce-Mn-NF and Ce-Mn-NC samples. All catalysts exhibited dominant component of lattice oxygen (O_{α}) species, together with a shoulder of surface adsorbed oxygen (O_{β}) species on the surface vacancies. The binding energy of 529.0–530.0 eV corresponded to O_{α} and the binding energy of 531.0–532.0 eV was ascribed to O_{β} . The integral ratio of $(O_{\beta}/O_{\alpha}+O_{\beta})$ was applied to estimate the concentration of adsorbed oxygen species (Table 2). Ce-Mn-NF and Ce-Mn-NC samples possess more surface adsorbed oxygen species compared with CeO₂-NF and CeO₂-NC, which indicate that Mn-doped CeO₂ contain more surface oxygen vacancy. Hence, it is inferred that the surface oxygen vacancy adsorbs and activates oxygen molecules to produce adsorbed oxygen species. This mechanism promotes the redox property of catalyst. A similar phenomenon was reported in the literature [34]. The O 1s XPS spectra results were in accordance with the XRD and Raman data.

Figure 5c presents the Mn 2p patterns of Ce-Mn-NF and Ce-Mn-NC. The binding energies of the Mn 2p_{3/2} component appear at 641.8 eV and those for Mn 2p_{1/2} appear at 653.5 eV. The spin orbit splitting is $\Delta E = 11.7$ eV and the width is 3.62 eV. According to literature data [35], the observed binding energy is tented to correspond to Mn₂O₃. It should be noted, though, that the BEs of various Mn ions are very close to each other, rendering impossible the exact identification of oxidation states due to overlap of the energy ranges for various oxidation states of Mn [26, 36]. In the Figure 5c, the Mn 2p_{3/2} XPS spectra were fitted by the presence of Mn²⁺, Mn³⁺ and Mn⁴⁺. The binding energy of 641.9–643 eV, 641.4–641.9 eV and 640.1–641.31 eV was ascribed to the peaks of Mn⁴⁺, Mn³⁺ and Mn²⁺ species [37], respectively.

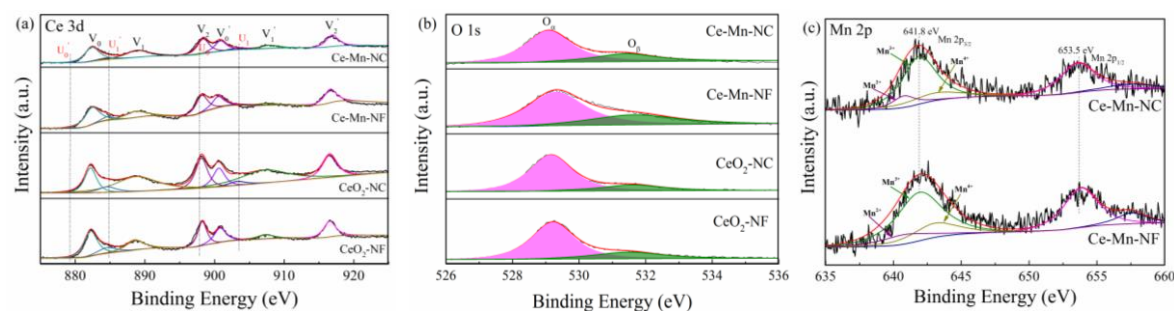


Figure 5. XPS spectra of various catalysts over the spectral regions of Ce 3d, O 1s and Mn 2p.

Table 2 Physical and chemical properties of all samples

Sample	A ₆₁₀ /A ₄₆₀ (%)	BE (eV)		O _β /(O _α +O _β)(%)	Ce ³⁺ /(Ce ³⁺ +Ce ⁴⁺)(%)	Mn 2p _{3/2} BE (eV)		
		O _α	O _β			Mn ⁴⁺	Mn ³⁺	Mn ²⁺
CeO ₂ -NF	13.9	529.2	531.5	21.1	8.74	—	—	—
Ce-Mn-NF	20.9	529.3	531.7	25.5	11.3	640.9	641.8	643.1
CeO ₂ -NC	11.3	529.2	531.6	17.1	7.32	—	—	—
Ce-Mn-NC	19.4	529.1	531.5	22.0	9.71	640.8	641.8	643.2

As mentioned above, oxygen vacancy correlates closely with the catalytic properties of CeO₂ and Mn-doped CeO₂. The distribution feature of oxygen vacancy can also be reflected through electron energy loss spectroscopy (EELS). The patterns of CeO₂ and Mn-doped CeO₂ are shown in Figure 6a, in which Mn L_{2,3}-edge and Ce M_{4,5}-edge spectra can be distinguished obviously. Through the Mn L_{2,3}-edge spectrum, it can be obtained that Mn ion exhibits mainly trivalent [38], which is consistent with the XPS data of Mn element. According to the literature [39-41], it can be acquired that the formation of oxygen vacancies is coupled with the localization delocalization effect of Ce 4f electrons. Therefore, the Ce M_{4,5}-edge EELS spectra were used to further investigate the distribution conditions of Ce³⁺ and oxygen vacancies (Figure 6b). The proportions of Ce³⁺ ([Ce³⁺]) were calculated via the M5/M4 white-line ratios for every sample [42]. The data show that the relative proportions of Ce³⁺ in Ce-Mn-NF (0.876) and Ce-Mn-NC (0.837) are more than those of CeO₂ with the same morphology (CeO₂-NF: 0.775, CeO₂-NC: 0.765) due to Mnⁿ⁺ replacing with some Ce⁴⁺, which indicate that abundant Ce³⁺ exists on the surface of Mn-doped CeO₂ and more oxygen vacancies are formed. The conclusion has also been identified by the results of Raman and XPS.

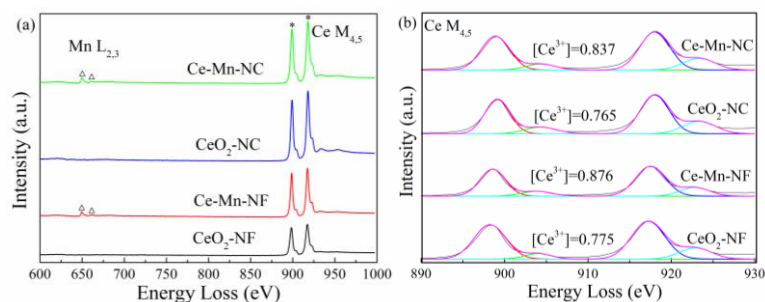


Figure 6. Ce $M_{4,5}$ -edge, Mn $L_{2,3}$ -edge EELS spectra (a) and Ce^{3+} distribution of CeO_2 samples (b).

EPR is sensitive to the paramagnetic species with unpaired electrons [43]. Thus, EPR spectra of the pure CeO_2 and Mn-doped CeO_2 samples were collected to study the oxygen vacancies and the species of reactive oxygen ($\cdot O_2$, \cdot^1O_2 and $\cdot OH$) [44, 45]. As presented in Figure 7a, pure- CeO_2 (CeO_2 -NF and CeO_2 -NC) exhibited two types of peaks of Ce^{3+} in terms of the surface ($g=1.965$) and bulk ($g=1.947$). After Mn doping, Mn-doped CeO_2 presented a strong EPR signal at $g=2.032$, ascribed to the combination of Mn ion with one or two electrons [46, 47]. The typical $\cdot O_2$ quartet spectrum, \cdot^1O_2 triplet spectrum and $\cdot OH$ spectrum can be detected for all the catalysts (Figure 7b-d). The intensities of peaks corresponding to $\cdot O_2$ and \cdot^1O_2 respectively in the Mn-doped CeO_2 catalyst are far higher than those of CeO_2 . This may be due to more Ce^{3+} to Ce^{4+} transition on the catalyst surface of Mn-doped CeO_2 , which provided many electrons to O_2 and accelerated the conversion of O_2 to active oxygen species. It is beneficial to accelerate the catalytic oxidation of benzene. It is worthy to note that CeO_2 only exhibits $\cdot OH$ characteristic quartet peaks, however Mn-doped CeO_2 contains other peaks attributed to oxidized DMPO (radical scavenger) besides $\cdot OH$ peaks, which indicate that Mn-doped CeO_2 possess higher oxidation ability (Figure 7d). Therefore, it is easier to catalytically oxidize benzene for Mn-doped CeO_2 . The EPR patterns of oxidized DMPO, labeled as DMPO-X can be seen in the Supporting Information.

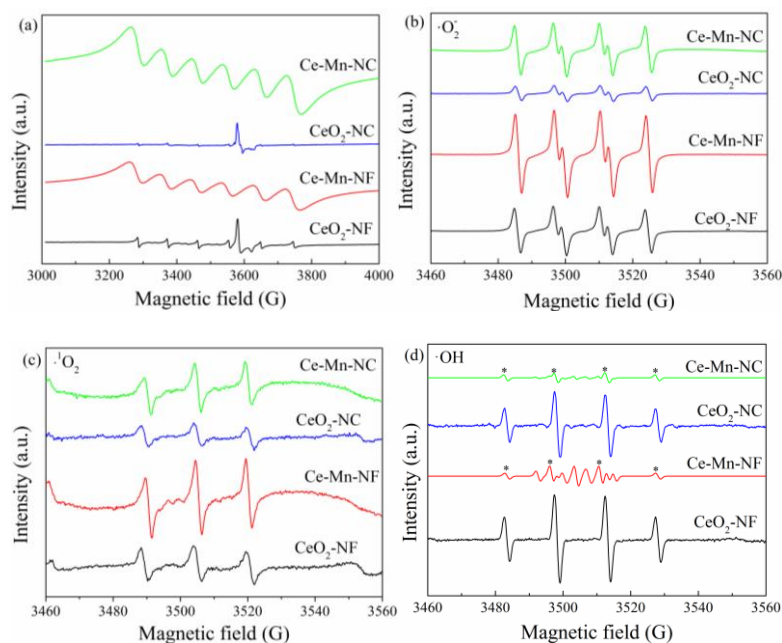


Figure 7. Electron paramagnetic resonance signals of all the samples (a), superoxide radical (b), singlet oxygen

(c) and hydroxyl radical (d).

The reducible surface oxygen species of CeO₂ and Mn-doped CeO₂ were studied using H₂-TPR as illustrated in Figure 8. The H₂-TPR measurement of CeO₂-NF exhibits two major reduction peaks at 478 °C and 725 °C. The two reduction peaks at 480 °C and 728 °C exist in the pattern of CeO₂-NC. According to the literature [48-50], the former low-temperature reduction (478 °C and 480 °C) is due to the removal of surface oxygen and the later high-temperature reduction (725 °C and 728 °C) is attributed to the release of oxygen species in bulk CeO₂. For Ce-Mn-NF, the TPR profile exhibits three overlapping peaks at lower temperature and one peak at higher temperature. The lower temperature peaks at 240 °C and 336 °C are assigned to the two-step reduction of Mn₂O₃ (Mn₂O₃ → Mn₃O₄; Mn₃O₄ → MnO) [51], while the reduction peak at 400 °C is corresponded to the reduction of surface oxygen in CeO₂. The higher temperature peak at 722 °C is attributed to the reduction of oxygen species in bulk CeO₂. The H₂-TPR pattern of Ce-Mn-NC is similar with that of Ce-Mn-NC. The lower temperature peaks (200 and 337 °C) correspond to the two-step reduction of Mn₂O₃. The peaks at 386 and 743 °C are attributed to the reduction of surface oxygen and bulk oxygen species in CeO₂, respectively. In addition, the reduction peaks of Mn-doped CeO₂ are shifted toward lower temperature compared with those of CeO₂, which indicate the reducibility of Mn-doped CeO₂ catalyst was increased due to Mn ion. Hence Mn-doped CeO₂ possess higher catalytic activities, which has been identified by the results of benzene oxidation.

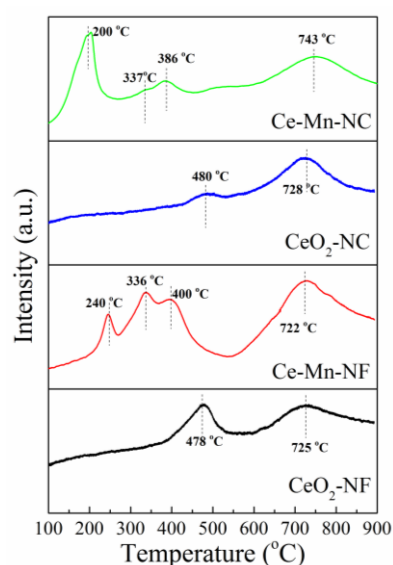


Figure 8. H₂-TPR profiles of CeO₂-NF, CeO₂-NC, Ce-Mn-NF and Ce-Mn-NC.

Through the analysis above, we have recognized that the oxygen vacancy has an important effect on their catalytic activities; however enough theory evidences are still needed. In this article, the density functional theory (DFT) is adopted to calculate the formation energy of oxygen vacancy so that identifying its role in the catalytic reaction further (Figure 9). The defect formation energy (E_f) of oxygen vacancy is defined as:

$$E_f = E_{s_{-v_o}} + \frac{1}{2}E_{O_2} - E_s \quad (4)$$

where $E_{s_{-v_o}}$ and E_s are the total energies of the supercell with and without an oxygen vacancy, and E_{O_2} is the total energy of an O_2 molecule [52].

We compare the oxygen vacancy formation energies (E_f) on the (110) and (100) crystal planes of Mn-doped CeO_2 . The calculated E_f corresponding to (110) plane is -0.48 eV. In contrast, the E_f on the (100) plane increases to 4.46 eV. The result means that the oxygen vacancy is easier to be formed on the (110) plane than (100) plane, which also indicate Mn ion is easier to be doped on the (110) plane. Given the central role of oxygen vacancy in catalyst [53, 54], the Ce-Mn-NF [exposed (110) and (100) planes] is therefore expected to show better performance than Ce-Mn-NC [exposed (100) plane] and pure CeO_2 (CeO_2 -NF and CeO_2 -NC), which is consistent with the results of benzene catalytic degradation. In addition, the distances of Ce-O near the oxygen vacancy in the Mn-doped CeO_2 , whether (110) or (100) planes, have only slight differences compared with those of CeO_2 which may be caused by the substitution of Mn ion. The distance data of Ce-O bond can be seen in Supporting Information.

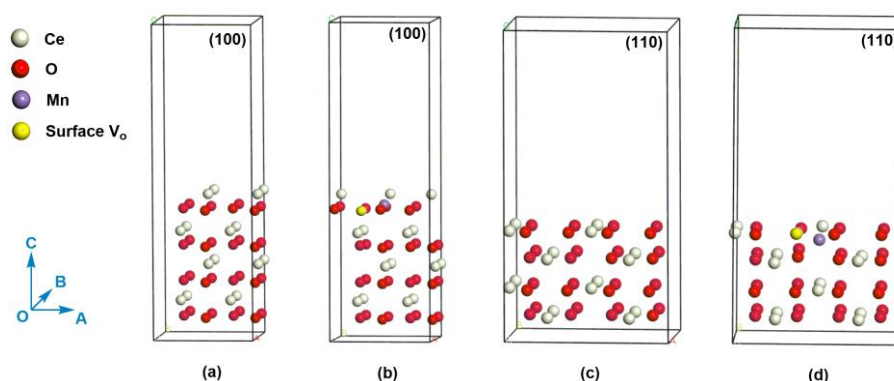


Figure 9. (a) (100) slab model for CeO_2 , (b) (100) slab model for Mn-doped CeO_2 with an oxygen vacancy, (c) (110) slab model for CeO_2 , (d) (110) slab model for Mn-doped CeO_2 with an oxygen vacancy. The white, red, purple, and yellow atoms refer to Ce atom, O atom, Mn atom, and surface oxygen vacancy, respectively.

3.3 Factor Influencing the Catalytic Activity

Through the analysis, it has been acquired that Mn-doped CeO_2 performs higher activity than pure CeO_2 with the same morphology over catalytic oxidation of benzene. Oxygen vacancy is considered to be a critical factor in catalytic performances. For Mn-doped CeO_2 , the existence of Ce-Mn solid solution results in the formation of more oxygen vacancies compared with CeO_2 due to incorporate Mn into CeO_2 crystal lattice, which can provide more surface active sites to adsorb active oxygen species. This phenomenon has also been identified through the analysis of TPR, in which Mn-doped CeO_2 possesses more highly reducible surface species closely related with surface oxygen vacancy. In addition, exposed crystal plane can also influence the catalytic activity, which is also attributed to the oxygen vacancy due to the different formation energy of oxygen vacancy on

the exposed crystal planes. Based on this, Ce-Mn-NF exhibits higher catalytic ability than Ce-Mn-NC.

As we known, the oxidation of organic molecules over transition metal oxide or mixed metal oxide catalysts involves two identical mechanisms: a Langmuir-Hinshelwood mechanism and a Mars-van Krevelen mechanism [55, 56]. At lower temperature, the adsorbed oxygen species with higher activity can enhance the adsorption and oxidation of VOCs, which match with Langmuir-Hinshelwood mechanism. It mainly contains four steps: (1) benzene molecule is adsorbed on the exposed crystal plane to form π -complex of benzene due to the interaction of benzene ring with catalyst; (2) gas-phase oxygen molecule is activated on the crystal plane to adsorb in surface vacancies; (3) the attack of active surface oxygen species to benzene ring; (4) benzene ring breakage and the formation of final products. When the reaction temperature rises, the adsorbed organic molecules are oxidized by the oxygen of metal oxides, which is consistent with the Mars-van Krevelen mechanism. It involves a similar process: (1) adsorption of benzene molecule; (2) the attack of lattice oxygen released from the catalyst to benzene ring; (3) benzene ring breakage and deep oxidation to final products. In addition, there are also two key elements involved in this process: (i) oxygen vacancies formed are replenished by the surface active oxygen species; (ii) active oxygen species are transported and delivered through the bulk oxygen vacancy (Figure 10). In summary, oxygen vacancy as transport medium, is the link of the whole reaction, therefore it has an important role in determining the catalytic activity.

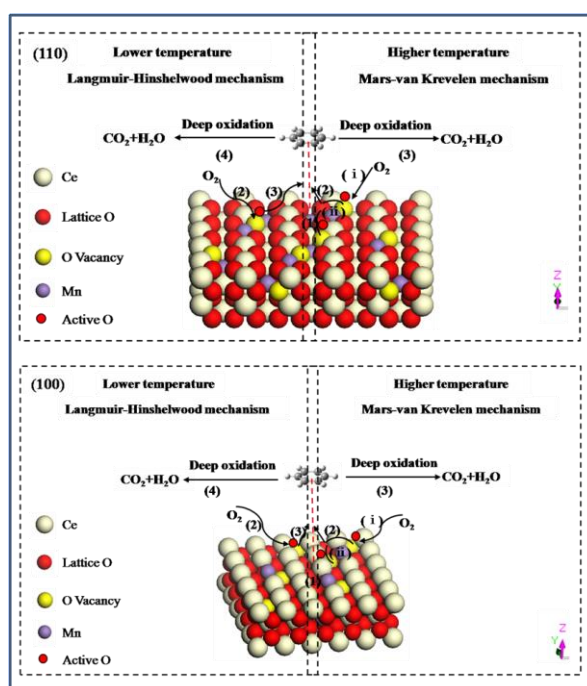


Figure 10. Proposed mechanism for benzene oxidation over Mn-doped CeO₂ on the different crystal plane.

4. Conclusions

Pure CeO₂ and Mn-doped CeO₂ with the same morphology (nanofiber and nanocube) were synthesized through hydrothermal method and the complete catalytic oxidation of benzene was examined. The results showed that Mn-doped CeO₂ possessed higher activity than pure CeO₂ with

the same morphology due to the formation of more oxygen vacancies. In the Mn-doped CeO₂, Ce-Mn-NF exhibited better catalytic behavior than Ce-Mn-NC, which was closely related the exposed crystal planes. Ce-Mn-NF exposed (110) and (100) planes, while Ce-Mn-NC exposed only (100) plane. According to theoretical calculation, the formation energy of oxygen vacancy on the (110) plane is much less than that on (100), which indicate that oxygen vacancy is easier formed and more surface active species is adsorbed on the (110) plane resulting in the higher catalytic property of Ce-Mn-NF. In general, the effect of crystal plane on the activity is also attributed to the oxygen vacancy. Therefore, oxygen vacancy is a key factor in the process of catalytic reaction.

Author Contributions: Conceptualization: Min Yang, Qi Wang, Zhen Wang; methodology: Min Yang, Genli Shen; software: Ke Deng.; validation: Min Yang, Yan Gong, Zhen Wang.; formal analysis: Min Yang; investigation: Min Yang, Mi Liu; resources: Zhen Wang, Qi Wang; data curation: Min Yang, Genli Shen; writing—original draft preparation: Min Yang; writing—review and editing: Yan Gong, Zhen Wang; visualization: Mi Liu; supervision: Yan Gong, Zhen Wang; project administration: Yunfa Chen.

Funding: This research was financially supported by the National Key R&D Program of China (2016YFC0207100).

Conflicts of Interest: The authors declare no conflict of interest.

References

1. Kong, J. J.; Xiang, Z. W.; Li, G. Y.; An, T. C. Introduce oxygen vacancies into CeO₂ catalyst for enhanced coke resistance during photothermocatalytic oxidation of typical VOCs. *Appl. Catal., B: Environ* **2020**, *269*, 118755.
2. Zhang, C. H.; Huang, H.; Li, G. Q.; Wang, L.; Song, L.; Li, X. B. Zeolitic acidity as a promoter for the catalytic oxidation of toluene over MnO_x/HZSM-5 catalysts. *Catal. Today* **2019**, *327*, 374-381.
3. Ma, C. Y.; Mu, Z.; Li, J. J.; Jin, Y. G.; Cheng, J.; Lu, G. Q.; Hao, Z. P.; Qiao, S. Z. Mesoporous Co₃O₄ and Au/Co₃O₄ Catalysts for Low-Temperature Oxidation of Trace Ethylene. *J. Am. Chem. Soc.* **2010**, *132*, 2608-2613.
4. Wang, Y. F.; Zhang, C. B.; Liu, F. D.; He, H. Well-dispersed palladium supported on ordered mesoporous Co₃O₄ for catalytic oxidation of o-xylene. *Appl. Catal., B: Environ* **2013**, *142*, 72-79.
5. Zhang, C. H.; Wang, C.; Zhan, W. C.; Guo, Y. L.; Guo, Y.; Lu, G. Z.; Baylet, A.; Giroir-Fendler, A. Catalytic oxidation of vinyl chloride emission over LaMnO₃ and LaB_{0.2}Mn_{0.8}O₃ (B = Co, Ni, Fe) catalysts. *Appl. Catal., B: Environ* **2013**, *129*, 509-516.
6. Kolodziej, A.; Lojewska, J.; Tyczkowski, J.; Jodlowski, P.; Redzyna, W.; Iwaniszyn, M.; Zapotoczny, S.; Kustrowski, P. Coupled engineering and chemical approach to the design of a catalytic structured reactor for combustion of VOCs: Cobalt oxide catalyst on knitted wire gauzes. *Chem. Eng. J.* **2012**, *200*, 329-337.
7. Mo, S. P.; Li, S. D.; Li, W. H.; Li, J. Q.; Chen, J. Y.; Chen, Y. F. Excellent low temperature performance for total benzene oxidation over mesoporous CoMnAl composited oxides from hydrotalcites. *J. Mater. Chem. A* **2016**, *4*, 8113-8122.
8. Zhao, L. L.; Zhang, Z. P.; Li, Y. S.; Leng, X. S.; Zhang, T. R.; Yuan, F. L.; Niu, X. Y.; Zhu, Y. J., Synthesis of Ce_aMnO_x hollow microsphere with hierarchical structure and its excellent catalytic performance for toluene combustion. *Appl. Catal., B: Environ* **2019**, *245*, 502-512.
9. Chang, Y. F.; McCarty, J. G. Novel oxygen storage components for advanced catalysts for emission

- control in natural gas fueled vehicles. *Catal. Today* **1996**, 30, 163-170.
10. Zhang, X. D.; Lv, X. T.; Bi, F. K.; Lu, G.; Wang, Y. X. Highly efficient Mn₂O₃ catalysts derived from Mn-MOFs for toluene oxidation: The influence of MOFs precursors. *Mol. Catal.* **2020**, 482, 110701.
 11. Zhou, G. L.; He, X. L.; Liu, S.; Xie, H. M.; Fu, M. Phenyl VOCs catalytic combustion on supported CoMn/AC oxide catalyst. *J. Ind. Eng. Chem.* **2015**, 21, 932-941.
 12. Xie, X. W.; Li, Y.; Liu, Z. Q.; Haruta, M.; Shen, W. J. Low-temperature oxidation of CO catalysed by Co₃O₄ nanorods. *Nature* **2009**, 458, 746-749.
 13. Trovarelli, A.; Llorca, J. Ceria Catalysts at Nanoscale: How Do Crystal Shapes Shape Catalysis? *ACS Catal.* **2017**, 7, 4716-4735.
 14. Lopez, J. M.; Gilbank, A. L.; Garcia, T.; Solsona, B.; Agouram, S.; Torrente-Murciano, L. The prevalence of surface oxygen vacancies over the mobility of bulk oxygen in nanostructured ceria for the total toluene oxidation. *Appl. Catal., B: Environ* **2015**, 174, 403-412.
 15. Yang, C. T.; Miao, G.; Pi, Y. H.; Xia, Q. B.; Wu, J. L.; Li, Z.; Xiao, J. Abatement of various types of VOCs by adsorption/catalytic oxidation: A review. *Chem. Eng. J.* **2019**, 370, 1128-1153.
 16. Weon, S.; Choi, W. TiO₂ Nanotubes with Open Channels as Deactivation-Resistant Photocatalyst for the Degradation of Volatile Organic Compounds. *Environ. Sci. Technol.* **2016**, 50, 2556-2563.
 17. Lin, R.; Liu, W. P.; Zhong, Y. J.; Luo, M. F. Catalyst characterization and activity of Ag-Mn complex oxides. *Appl. Catal., A: Gen* **2001**, 220, 165-171.
 18. Quiroz, J.; Giraudon, J. M.; Gervasini, A.; Dujardin, C.; Lancelot, C.; Trentesaux, M.; Lamonier, J. F. Total Oxidation of Formaldehyde over MnO_x-CeO₂ Catalysts: The Effect of Acid Treatment. *Acs Catal.* **2015**, 5, 2260-2269.
 19. Qi, G. S.; Yang, R. T.; Chang, R. MnO_x-CeO₂ mixed oxides prepared by co-precipitation for selective catalytic reduction of NO with NH₃ at low temperatures. *Appl. Catal., B: Environ* **2004**, 51, 93-106.
 20. Qi, G. S.; Yang, R. T. Performance and kinetics study for low-temperature SCR of NO with NH₃ over MnO_x-CeO₂ catalyst. *J. Catal.* **2003**, 217, 434-441.
 21. Guo, Z. Y.; Liang, Q. H.; Yang, Z. Y.; Liu, S.; Huang, Z. H.; Kang, F. Y. Modifying porous carbon nanofibers with MnO_x-CeO₂-Al₂O₃ mixed oxides for NO catalytic oxidation at room temperature. *Catal. Sci. Technol.* **2016**, 6, 422-425.
 22. Zhang, J.; Cao, Y. D.; Wang, C. A.; Ran, R. Design and Preparation of MnO₂/CeO₂-MnO₂ Double-Shelled Binary Oxide Hollow Spheres and Their Application in CO Oxidation. *ACS Appl. Mater. Inter.* **2016**, 8, 8670-8677.
 23. Xing, L. L.; Yang, Y. X.; Cao, C. M.; Zhao, D. Y.; Gao, Z. N.; Ren, W.; Tian, Y.; Ding, T.; Li, X. G. Decorating CeO₂ Nanoparticles on Mn₂O₃ Nanosheets to Improve Catalytic Soot Combustion. *ACS Sustainable Chem. Eng.* **2018**, 6, 16544-16554.
 24. Xiao, W. D.; Guo, Q. L.; Wang, E. G. Transformation of CeO₂(111) to Ce₂O₃(0001) films. *Chem. Phys. Lett.* **2003**, 368, 527-531.
 25. Lenormand, F.; Hilaire, L.; Kili, K.; Krill, G.; Maire, G. Oxidation-State of Cerium in Cerium-Based Catalysts Investigated by Spectroscopic Probes. *J. Phys. Chem.* **1988**, 92, 2561-2568.
 26. Dula, R.; Janik, R.; Machej, T.; Stoch, J.; Grabowski, R.; Serwicka, E. M. Mn-containing catalytic materials for the total combustion of toluene: The role of Mn localisation in the structure of LDH precursor. *Catal. Today* **2007**, 119, 327-331.
 27. Weber, W. H.; Hass, K. C.; McBride, J. R., Raman-Study of CeO₂ - 2nd-Order Scattering, Lattice-Dynamics, and Particle-Size Effects. *Phys. Rev. B* **1993**, 48, 178-185.
 28. Hu, F. Y.; Chen, J. J.; Peng, Y.; Song, H.; Li, K. Z.; Li, J. H., Novel nanowire self-assembled hierarchical

- CeO₂ microspheres for low temperature toluene catalytic combustion. *Chem. Eng. J.* **2018**, 331, 425-434.
29. Du, X. J.; Zhang, D. S.; Shi, L. Y.; Gao, R. H.; Zhang, J. P. Morphology Dependence of Catalytic Properties of Ni/CeO₂ Nanostructures for Carbon Dioxide Reforming of Methane. *J. Phys. Chem. C* **2012**, 116, 10009-10016.
 30. Souza, E. C. C.; Brito, H. F.; Muccillo, E. N. S. Optical and electrical characterization of samaria-doped ceria. *J. Alloys Compd.* **2010**, 491, 460-464.
 31. Pfau, A.; Schierbaum, K. D. The electronic-structure of stoichiometric and reduced CeO₂ surfaces - an XPS, UPS and HREELS study. *Surf. Sci.* **1994**, 321, 71-80.
 32. Du, X. S.; Wang, X. M.; Chen, Y. R.; Gao, X.; Zhang, L. Supported metal sulfates on Ce-TiO_x as catalysts for NH₃-SCR of NO: High resistances to SO₂ and potassium. *J. Ind. Eng. Chem.* **2016**, 36, 271-278.
 33. Lee, S. M.; Park, K. H.; Hong, S. C. MnO_x/CeO₂-TiO₂ mixed oxide catalysts for the selective catalytic reduction of NO with NH₃ at low temperature. *Chem. Eng. J.* **2012**, 195, 323-331.
 34. Yang, W. H.; Su, Z. A.; Xu, Z. H.; Yang, W. N.; Peng, Y.; Li, J. H. Comparative study of α -, β -, γ - and δ -MnO₂ on toluene oxidation: Oxygen vacancies and reaction intermediates. *Appl. Catal., B: Environ* **2020**, 260, 118150.
 35. Machida, M.; Uto, M.; Kurogi, D.; Kijima, T. MnO_x-CeO₂ binary oxides for catalytic NO_x sorption at low temperatures. Sorptive removal of NO_x. *Chem. Mater.* **2000**, 12, 3158-3164.
 36. Rao, T.; Shen, M. Q.; Jia, L. W.; Hao, J. J.; Wang, J. Oxidation of ethanol over Mn-Ce-O and Mn-Ce-Zr-O complex compounds synthesized by sol-gel method. *Catal. Commun.* **2007**, 8, 1743-1747.
 37. Ramirez, A.; Hillebrand, P.; Stellmach, D.; May, M. M.; Bogdanoff, P.; Fiechter, S. Evaluation of MnO_x, Mn₂O₃, and Mn₃O₄ Electrodeposited Films for the Oxygen Evolution Reaction of Water. *J. Phys. Chem. C* **2014**, 118, 14073-14081.
 38. Marris, H.; Deboudt, K.; Flament, P.; Grobety, B.; Giere, R. Fe and Mn Oxidation States by TEM-EELS in Fine-Particle Emissions from a Fe-Mn Alloy Making Plant. *Environ. Sci. Technol.* **2013**, 47, 10832-10840.
 39. Hao, X. D.; Yoko, A.; Chen, C. L.; Inoue, K.; Saito, M.; Seong, G.; Takami, S.; Adschiri, T.; Ikuhara, Y. Atomic-Scale Valence State Distribution inside Ultrafine CeO₂ Nanocubes and Its Size Dependence. *Small* **2018**, 14, 1802915.
 40. Paier, J.; Penschke, C.; Sauer, J. Oxygen Defects and Surface Chemistry of Ceria: Quantum Chemical Studies Compared to Experiment. *Chem. Rev.* **2013**, 113, 3949-3985.
 41. Hojo, H.; Mizoguchi, T.; Ohta, H.; Findlay, S. D.; Shibata, N.; Yamamoto, T.; Ikuhara, Y. Atomic Structure of a CeO₂ Grain Boundary: The Role of Oxygen Vacancies. *Nano Lett.* **2010**, 10, 4668-4672.
 42. Su, Z. A.; Yang, W. H.; Wang, C. Z.; Xiong, S. C.; Cao, X. Z.; Peng, Y.; Si, W. Z.; Weng, Y. B.; Xue, M.; Li, J. H. Roles of Oxygen Vacancies in the Bulk and Surface of CeO₂ for Toluene Catalytic Combustion. *Environ. Sci. Technol.* **2020**, 54, 12684-12692.
 43. Zhang, H.; Cai, J. M.; Wang, Y. T.; Wu, M. Q.; Meng, M.; Tian, Y.; Li, X. G.; Zhang, J.; Zheng, L. R.; Jiang, Z.; Gong, J. L. Insights into the effects of surface/bulk defects on photocatalytic hydrogen evolution over TiO₂ with exposed {001} facets. *Appl. Catal., B: Environ* **2018**, 220, 126-136.
 44. Ren, S.; Liang, W. J.; Li, Q. L.; Zhu, Y. X., Effect of Pd/Ce loading on the performance of Pd-Ce/ γ -Al₂O₃ catalysts for toluene abatement. *Chemosphere* **2020**, 251, 126382.
 45. Xia, D. H.; Xu, W. J.; Wang, Y. C.; Yang, J. L.; Huang, Y. J.; Hu, L. L.; He, C.; Shu, D.; Leung, D. Y. C.; Pang, Z. H. Enhanced Performance and Conversion Pathway for Catalytic Ozonation of Methyl Mercaptan on Single-Atom Ag Deposited Three-Dimensional Ordered Mesoporous MnO₂. *Environ. Sci. Technol.* **2018**, 52, 13399-13409.
 46. Qi, G. S.; Yang, R. T. Characterization and FTIR studies of MnO_x-CeO₂ catalyst for low-temperature

- selective catalytic reduction of NO with NH₃. *J. Phys. Chem. B* **2004**, 108, 15738-15747.
47. Yu, X. L.; Wu, X. M.; Chen, Z. Y.; Huang, Z. W.; Jing, G. H. Oxygen vacancy defect engineering in Mn-doped CeO₂ nanostructures for, nitrogen oxides emission abatement. *Mol. Catal.* **2019**, 476, 110512.
 48. Trovarelli, A. Catalytic properties of ceria and CeO₂-containing materials. *Catal. Rev.* **1996**, 38, 439-520.
 49. Aneggi, E.; Boaro, M.; de Leitenburg, C.; Dolcetti, G.; Trovarelli, A. Insights into the redox properties of ceria-based oxides and their implications in catalysis. *J. Alloys Compd.* **2006**, 408, 1096-1102.
 50. Tana; Zhang, M. L.; Li, J.; Li, H. J.; Li, Y.; Shen, W. J. Morphology-dependent redox and catalytic properties of CeO₂ nanostructures: Nanowires, nanorods and nanoparticles. *Catal. Today* **2009**, 148, 179-183.
 51. Wang, Z.; Shen, G. L.; Li, J. Q.; Liu, H. D.; Wang, Q.; Chen, Y. F. Catalytic removal of benzene over CeO₂-MnO_x composite oxides prepared by hydrothermal method. *Appl. Catal., B: Environ* **2013**, 138, 253-259.
 52. Wang, Z.; Deng, Y. Z.; Shen, G. L.; Akram, S.; Han, N.; Chen, Y. F.; Wang, Q. Catalytic Degradation of Benzene over Nanocatalysts containing Cerium and Manganese. *Chemistryopen* **2016**, 5, 495-504.
 53. Blochl, P. E. Projector Augmented-Wave Method. *Phys. Rev. B* **1994**, 50, 17953-17979.
 54. Chang, S. J.; Li, M.; Hua, Q.; Zhang, L. J.; Ma, Y. S.; Ye, B. J.; Huang, W. X. Shape-dependent interplay between oxygen vacancies and Ag-CeO₂ interaction in Ag/CeO₂ catalysts and their influence on the catalytic activity. *J. Catal.* **2012**, 293, 195-204.
 55. Santos, V. P.; Pereira, M. F. R.; Orfao, J. J. M.; Figueiredo, J. L. The role of lattice oxygen on the activity of manganese oxides towards the oxidation of volatile organic compounds. *Appl. Catal., B: Environ* **2010**, 99, 353-363.
 56. Tang, W. X.; Wu, X. F.; Li, D. Y.; Wang, Z.; Liu, G.; Liu, H. D.; Chen, Y. F. Oxalate route for promoting activity of manganese oxide catalysts in total VOCs' oxidation: effect of calcination temperature and preparation method. *J. Mater. Chem. A* **2014**, 2, 2544-2554.